De novo design of dual-topology membrane transporters

Xi Chen[1,2,3,4*], Xiaofeng Zhou[2,3*], Jiawei Zhou[2,3], Tengyu Xie [2,3], Yaning Li[2,3,4], Yuxuan Yan[2,3], Jing Huang[2,3], Zibo Chen[2,3#], Dan Ma[2,3#], Peilong Lu[2,3,4#]

[1]School of Life Sciences, Fudan University, Shanghai, 200438, China.

[2]State Key Laboratory of Gene Expression, Key Laboratory of Structural Biology of Zhejiang Province, School of Life Sciences and Research Center for Industries of the Future, Westlake University, Hangzhou, Zhejiang, 310024, China

[3]Institute of Biology, Westlake Institute for Advanced Study, Hangzhou, Zhejiang, 310024, China

[4]New Cornerstone Science Laboratory, Hangzhou, Zhejiang, 310024, China

*These authors contributed equally to this work

#Corresponding authors. Email: lupeilong@westlake.edu.cn; madan@westlake.edu.cn; zibochen@westlake.edu.cn

Key Words: *de novo* protein design; deep learning; parametric design; transmembrane protein; membrane transport; transporter; dual topology; dynamic; cryo-EM.

Abstract

The transport of molecules across biological membranes is essential for life, allowing cells to acquire nutrients, remove waste, maintain cellular homeostasis and communicate with their environment[1,2]. Although there have been advances in de novo design of functional transmembrane proteins[3-15], designing synthetic transporters that robustly and selectively transport specific small molecules across membranes has remained a significant challenge[3,8,16,17]. In this study, we present the de novo design of dual-topology membrane transporters that achieve substrate-specific transport through a rationally programmed conformational cycle. By integrating symmetric backbone assembly with deep learning–guided sequence optimization, we designed 3-TM proteins that insert in opposite orientations and assemble into antiparallel dimers, forming a putative central substrate binding site that enables alternating access to either side of the membrane. These designed transporters mediate selective uptake of small-molecule dyes in both living cells and artificial liposomes, driven by substrate concentration gradients, resembling those of natural uniporters. Cryo-EM structures reveal high fidelity to the design models, and functional assays corroborate the dual-topology architecture and mechanism of action. Here we show that functional, dynamic membrane transporters can be built from the ground up with atomic-level precision—providing insights into the evolutionary origins of transporters and opening new avenues for applications, including targeted drug delivery and metabolic pathway engineering.

Membrane transporters are essential to cellular physiology, mediating the selective translocation of ions, metabolites, and a wide range of drug molecules across lipid bilayers, enabling cells to maintain homeostasis, generate energy, and communicate with their environment[1,18,19]. De novo design of membrane transporters may advance membrane biology by providing models to elucidate the fundamental mechanisms of membrane transport, allow for the engineering of custom pathways for chemical uptake and export in cell factories, and enable targeted drug delivery. Despite advances in the de novo design of transmembrane proteins[3-15], the design of functional small-molecule membrane transporters with precisely defined three-dimensional structures, controlled membrane topology, specific substrate recognition, and regulated dynamic conformational changes remains a significant challenge[3,8,16,17].

Designing functional transporters requires the design of a dynamic protein structural landscape rather than a single static conformation, as transporters undergo large-scale conformational changes—such as transitions between inward-facing, occluded, and outward-facing states—to facilitate substrate translocation across membranes[1,18-20]. This functional cycle is governed by the relative energies and interconversion rates among these states, which collectively define the conformational energy landscape. We propose that structured dual-topology membrane transporters[21]—proteins capable of inserting into the membrane in two opposite orientations and assembling into a functional antiparallel dimer, exemplified by the multidrug transporter EmrE[20]—offer a simplified prototype for transporter design.

Due to the intrinsic symmetry of the dual-topology architecture, the inward- and outward-facing conformational states of these transporters possess comparable free energy levels (Fig. 1a). Consequently, designing a single, energetically favorable, symmetric occluded state with ligand bound could lower the energy barrier for ligand translocation across the membrane and promote similar propensities for switching to either the inward- or outward-facing conformation. The energy gaps between the ligand-bound occluded state and the two states open to either side are balanced within the thermal energy range, enabling efficient alternating access without requiring additional energy input (Fig. 1a). Ligand entry into the binding site from solution may be realized through thermodynamics-driven breathing motions of the protein, as indicated in the designed ligand-binding transmembrane fluorescence-activating protein (tmFAP)[6]—the ligand binding site is entirely shielded from solvent, requiring conformational changes in the protein to allow ligand

access. Since the inward- and outward-facing conformations were not explicitly designed, multiple transient conformations may exist; however, they are expected to occur in symmetric pairs.

In the programmed conformational cycle, substrate transport is driven solely by the substrate concentration gradient across the membrane. Substrate binding from the high-concentration side induces formation of the ligand-bound occluded state, which then undergoes a conformational transition leading to substrate release on the low-concentration side, enabling passive, gradient-driven transport (Fig. 1a). This mechanism exploits the intrinsic symmetry and conformational dynamics of the dual-topology architecture to achieve directional transport through thermodynamically favorable substrate diffusion, effectively mimicking the natural uniporters[1,19,20].

Design of 3-TM dual-topology transporters for a dye substrate

We de novo designed dual-topology membrane transporters using symmetric backbone assembly combined with sequence optimization driven by deep neural network. We aimed to design a 3-transmembrane (3-TM) antiparallel dimer as a minimal transporter (Fig. 1b), as 3-TM proteins can form larger ligand-binding sites and exhibit greater structural diversities than 2-TM proteins. To our knowledge, this architecture has not been employed by natural transporters[19]. To design the symmetric occluded state, we first generated six-helix bundle backbones with C2 symmetry using parametric equations[22-24], incorporating a central pocket suitable for accommodating a substrate. We selected the dye molecule Cy3 (DiSO3, DI Et) (abbreviated as Cy3, molecular weight 544.68 Da) as the target small molecule substrate (Fig. 1c). Due to its high polarity, Cy3 cannot permeate cell membrane (Fig. 2). Moreover, its near-symmetrical structure simplifies the design process: aligning the symmetry axes of the protein backbone and the small molecule reduces the conformational search space to only two parameters—rotation around and translation along the C2 symmetry axis. We placed Cy3 in the central pocket of the helical bundle scaffolds (Fig. 1c) and employed Rosetta for iterative protein–ligand interface sampling and design, optimizing interaction energy and ligand shape complementarity. We further used ProteinMPNN[25] to design the whole protein sequence while keeping the ligand interacting residues fixed.

To achieve dual-topology membrane insertion, we incorporated two rings of amphipathic aromatic residues at the designed lipid–water interface (Fig. 1d), positioned on the extracellular and

periplasmic sides, and balanced the distribution of positively charged residues on both sides to bypass the positive-inside rule, which dictates that positively charged residues preferentially localize to the cytoplasmic side[26]. During Rosetta-based sequence design[9], the surface residues between these two rings were constrained to hydrophobic amino acids. Designed sequences were computationally filtered based on prediction confidence and structural similarity between the designed and AlphaFold2[27]-predicted models. Additionally, TMHMM 2.0[28] was used to select monomeric designs predicted to contain three transmembrane helices and to exhibit an N-terminal cytoplasmic orientation with a probability of 0.5 ± 0.2, indicating a similar chance for the N-terminal to adopt extracellular orientation and thus high likelihood of dual topology. In contrast, previously designed N-terminal cytoplasmic membrane proteins typically exhibit probability values closed to 1.0. We used Autodock Vina[29] to dock Cy3 to the design models to assess their pockets. The binding mode in the top output from Vina docking closely matched that in each design model, indicating that the pocket organization was suitable for effective binding of substrate.

Functional screening

Genes encoding 50 selected transporter designs were synthesized and expressed in *E. coli*. In a cell-based substrate uptake assay, 25 designs showed robust Cy3 dye accumulation, exceeding the control (unrelated structural protein TMHC2) by more than about 13-fold (Fig. 2a-c). To investigate the substrate specificity of the designed transporters, we randomly selected 11 designs from those exhibiting robust Cy3 transport, and evaluated their ability to transport several small-molecule dyes with diverse chemical structures (Fig. 2d). The uptake of a modified Cy3 analogue Cy3 DiAcid (DiSO3) (abbreviated as Cy3 DA, molecular weight 716.86 Da)—structurally much larger than Cy3—was minimal across all 11 designs, similar to the limited uptake observed for structurally distinct fluorophores such as Lucifer yellow (molecular weight 428.4 Da for the dye anion) and Calcein (molecular weight 622.5 Da). Taken together, these results suggest that the designs exhibited substrate-specific transport activity in the cell-based uptake assay.

Structural validation

We subsequently attempted cryo-electron microscopy (cryo-EM) structure determination despite the small size of the transporters. To increase particle size to facilitate cryo-EM analysis, we employed three distinct protein engineering strategies: replacing one loop between two adjacent TM helices with either the BRIL domain or a de novo designed rigid soluble domain, or fusing an

N-terminal maltose-binding protein (MBP) that is further stabilized by a C-terminal MBP binding designed ankyrin-repeat protein (DARPin) domain. Throughout these engineering, the sequence of the remainder of the designed transporter was kept unchanged. All engineered variants were expressed and purified to homogeneity using nickel-affinity chromatography followed by size-exclusion chromatography (SEC).

We determined the cryo-EM structures of Trans25-sol and Trans42-MBP at resolutions of 2.93 and 3.40 Å, respectively (Fig. 3). Notably, the transmembrane domains of both designs closely matched their corresponding design models, with Cα root-mean-square deviations (RMSDs) of 1.2 and 0.5 Å for all aligned residues (Fig. 3). The cryo-EM maps both revealed six transmembrane helices arranged into roughly antiparallel C2 symmetry, surrounded by densities likely originating from detergent molecules. For Trans42-MBP, the EM map and 2D class averages revealed soluble domain density on only one side of the membrane, with weak density observed on the opposite side. The medium-resolution cryo-EM map resolved the transmembrane domain, along with one MBP and one DARPin domain assembled into a complex (Fig. 3d-e).

Although Trans25 was fused to the appended soluble domain, the resulting Trans25-sol construct retained substrate transport activity in the *E. coli*-based dye accumulation assay. 2D class averages revealed a clear C2-symmetric protein structure for Trans25-sol, enabling high-resolution 3D reconstruction. The resulting density map clearly resolved the transmembrane domain as well as the two de novo designed rigid soluble domains positioned on opposite sides of the membrane (Fig. 3a). The cryo-EM structure of Trans25-sol reveals a central cavity at the dimer interface within the membrane, which is likely the substrate-binding site (Fig. 3c). At the dimer interface, TM1 of one protomer interacts with the inverted TM1 of the other protomer, while TM3s were similarly paired, completing the circular assembly. The TM1 interface is predominantly hydrophobic, whereas the TM3 interface features two hydrogen bonds with side chains of tryptophan residues (W366 in Trans25-sol) serving as the donor and main-chain carbonyl oxygen as the acceptor—interactions commonly observed in native membrane proteins but rarely found in de novo designed systems.

Although the putative ligand-binding cavity in Trans25 is accessible to solvent from both sides of the membrane, the connecting channels are highly constricted, with a minimal radius of approximately 1.3 Å. These constricted regions would likely prevent the free diffusion of small-

molecule ligands unless conformational changes occur during transitions between different structural states. To assess whether this structure can accommodate the transport substrate, we docked the Cy3 ligand into the Trans25-sol cryo-EM model. The results indicate that Cy3 can fit within the central pathway and closely aligns with its position in the design model.

Functional characterization

Both Trans25 and Trans42 exhibited time- and concentration-dependent accumulation of Cy3 in the cell-based transport assay (Fig. 4a, b). Expression of the designed transporters in *E. coli* enabled rapid uptake of Cy3, with accumulation reaching a plateau within one hour. Kinetic analysis of maximal transport velocity (V_{max}) and Michaelis constant (K_m) revealed that the estimated Cy3 transport kinetics for Trans25 are within the range typical of known transporters (Fig. 4c). We developed a substrate transport competition assay employing both Cy3 and Lucifer yellow dyes concurrently in the same solution to rigorously evaluate substrate specificity (Fig. 4d). The results show that the engineered transporters Trans25 and Trans42 selectively transport Cy3, but not Lucifer yellow, suggesting that the observed uptake is both specific and dependent on the designed transport path.

To validate the designed protein–ligand interactions in Trans25 and Trans42, we systematically introduced point mutations within the designed transport pathway and assessed their functional impact (Fig. 4e, f). Substituting nonpolar residues with negatively charged ones in Trans25 largely abolished substrate transport, highlighting the importance of these putative ligand-binding residues (Fig. 4e). To enable targeted chemical modification, we generated the trans42_I7C mutant, in which a key residue was replaced with cysteine; this variant retained robust Cy3 accumulation in *E. coli* cells, indicating preserved transporter function. We then exploited the reactivity of the introduced cysteine to test sulfhydryl-specific blockers, finding that treatment with methanethiosulfonate (MTSES) significantly reduced Cy3 uptake in the trans42_I7C mutant (Fig. 4f). This inhibition was strictly dependent on the engineered cysteine, as MTSES had no effect on the transport activity of original Trans42 design lacking the residue. To assess potential structural perturbations, we expressed and purified all variants from *E. coli*, and observed minimal differences in complex assembly and solution behavior, supporting that the mutations specifically affect transport function rather than overall folding. Together, the mutagenesis, chemical modification, and biochemical analyses validate the designed transport path, confirm the

functional relevance of the central cavity, and identify key residues critical for substrate translocation. These results are consistent with the structural data, collectively suggesting that ligand transport occurs through the rationally designed path rather than through non-selective pores.

In vitro transport

To evaluate the *in vitro* transport activity of these de novo designed transporters, we employed a cell-free expression system within Giant Unilamellar Vesicles (GUVs). Plasmids encoding the target proteins were co-encapsulated with the PUREfrex system[30] and Cy3 dye inside GUVs generated via the inverted emulsion method[31]. We hypothesized that the continuous expression and subsequent membrane insertion of functional transporters would facilitate Cy3 efflux, resulting in a time-dependent decay of intra-vesicular fluorescence (Fig. 5a).

Indeed, GUVs expressing Trans25 and Trans42 exhibited a marked reduction in Cy3 fluorescence compared to the non-functional control (TMHC2) (Fig. 5b, c). To confirm that dye leakage was transporter-mediated, we tested non-functional mutants of Trans25 and observed no fluorescence decrease (Fig. 5d, e). Furthermore, Trans42 and its I7C mutant displayed MTSES sensitivity comparable to that observed in the cell-based uptake assays (Fig. 5f, g). Collectively, these results demonstrate the functionality of these designed transporters across diverse experimental settings.

Dual-topology

To validate the dual-topology design, split-GFP complementation[32] was employed in *E. coli* (Fig. 6a). Trans25 and Trans42, each tagged with GFP11 at the N-terminus and GFP1–10 at the C-terminus, exhibited strong fluorescence, indicating that both termini are positioned on the same side of the membrane—a hallmark of dual-topology insertion. In contrast, control constructs, including those bearing only the GFP11 tag, only the GFP1–10 tag, or the single-topology 3-TM designer channel dVGAC[5] dual-tagged with GFP11 (N-terminus) and GFP1–10 (C-terminus), showed minimal fluorescence. Fluorescence imaging further confirmed the membrane-localization of Trans25 and Trans42 bearing both GFP11 and GFP1–10 tags.

We further examined the influence of eGFP tag position on substrate transport (Fig. 6b). All eGFP-fused constructs were expressed and showed substantial fluorescent signals of eGFP on cell membrane. When Trans25 and Trans42 were tagged with eGFP at the C-terminus, dye transport

remained unaffected. In contrast, N-terminal eGFP tagging of these proteins abolished dye transport. These results indicate that an N-terminal eGFP tag interferes with the formation of the N-out topology in the dual topology transporters.

The 3-TM dual-topology architecture allows for the direct fusion of the two protomers into a single-chain construct (Fig. 6c). To minimize linker-induced disruptions to the symmetric architecture and preserve the relative energy levels of the assembly, the protomers in the single-chain variants are linked by a flexible Gly-Ser spacer. Single-chain designs Trans25 and Trans42 demonstrated robust dye transport in cell-based uptake assays similar to the original design. These results together demonstrate that Trans25 and Trans42 insert in opposite orientations and assemble into antiparallel dimers, thereby validating the designed model and the cryo-EM structures.

Discussions

Unlike designed proteins with overall static structural conformation, our de novo designed transporters achieved dynamic structural transitions. By computationally stabilizing a symmetric, ligand-bound occluded state, the design leverages thermodynamic and chemical gradient to drive substrate transport, mimicking passive uniporters. The central ligand binding pocket, constricted in the occluded state, requires conformational "breathing" or rocking motions for ligand entry and release—dynamics reminiscent of natural transporters. The dual-topology architecture—where monomers insert in opposite orientations to form antiparallel dimers—rarely seen in natural transporters as there are only a few cases such as EmrE, enabling coordinated rocking motions that facilitate directional transport. The biochemical and cryo-EM data are in close agreement with the designed models. This symmetry-driven mechanism simplifies the design of conformational change and offers a scalable framework for designing and evolving more complex, controllable transporters with programmable substrate preference.

An intriguing question in the evolution of membrane transporters is how complex membrane transporters arose from simpler precursors. Many natural transporters, including members of the 12-transmembrane (12-TM) major facilitator superfamily (MFS)[20,33,34], exhibit structurally similar 3-TM inverted repeats related by 180° rotational pseudosymmetry within the membrane plane. This structural organization strongly suggests that MFS transporters evolved through gene duplication and fusion of primordial 3-TM dual-topology protein modules. The odd number of

transmembrane helices—such as three—facilitates such fusion by positioning the N-terminus of one protomer on the same side of the membrane as the C-terminus of the other, enabling proper alignment. In contrast, transporters with an even number of transmembrane helices require an additional linker helix to achieve functional dimerization. Evolutionary pressures likely favored these fusions to broaden substrate specificity and enhance coupling between substrate binding and translocation. Despite the strength of this hypothesis, no natural 3-TM dual-topology ancestral transporter has been identified to date. Our results, from a de novo design perspective, bridge this gap by demonstrating that a minimal, symmetric 3-TM dual-topology protein can stably fold within the membrane and mediate directional, substrate-specific transport—offering a viable model for the long-postulated evolutionary precursor. This hypothesis is further supported by the single-chain variants of the dual-topology designs that showed robust dye transport activity.

The de novo design of dynamic membrane transporters represents an advance in protein design, providing not only a novel class of synthetic biological tools but also deeper insights into the fundamental principles underlying membrane protein evolution, dynamics, and function. While prior studies have elegantly achieved de novo design of the 25-residue Rocker peptide capable of zinc transport[11]—our transporters are genetically encoded, expressed in living cells, and capable of specifically transporting small molecules rather than zinc ion. The selective transport of artificial compounds such as Cy3 demonstrates that these systems can be precisely designed for specific small molecule substrates, enabling the import and export of valuable chemicals in cell factories integrated with engineered metabolic pathways, or facilitating the targeted delivery of small-molecule therapeutics to specific tissues or cell types expressing the designer transporters. Our designer transporters demonstrate high structural accuracy, functional complexity, and kinetic performance, representing a significant advance toward achieving custom-tailored functionalities compatible with living organisms through de novo protein design.

References

1 Yan, N. Structural Biology of the Major Facilitator Superfamily Transporters. *Annual Review of Biophysics* **44**, 257-283 (2015).

2 Shi, Y. Common folds and transport mechanisms of secondary active transporters. *Annu Rev Biophys* **42**, 51-72 (2013).

3 Zhou, C. & Lu, P. De novo design of membrane transport proteins. *Proteins* **90**, 1800-1806 (2022).

4 Zhu, J. & Lu, P. Computational design of transmembrane proteins. *Current Opinion in Structural Biology* **74**, 102381 (2022).
5 Zhou, C. *et al.* De novo designed voltage-gated anion channels suppress neuron firing. *Cell* **188**, 7495-7511.e7421 (2025).
6 Zhu, J. *et al.* De novo design of transmembrane fluorescence-activating proteins. *Nature* **640**, 249-257 (2025).
7 Liu, Y. *et al.* Bottom-up design of Ca(2+) channels from defined selectivity filter geometry. *Nature* **648**, 468-476 (2025).
8 Joh, N. H., Grigoryan, G., Wu, Y. & DeGrado, W. F. Design of self-assembling transmembrane helical bundles to elucidate principles required for membrane protein folding and ion transport. *Philosophical Transactions of the Royal Society B: Biological Sciences* **372**, 20160214-20160214 (2017).
9 Lu, P. *et al.* Accurate computational design of multipass transmembrane proteins. *Science* **359**, 1042-1046 (2018).
10 Xu, C. *et al.* Computational design of transmembrane pores. *Nature* **585**, 129-134 (2020).
11 Joh, N. H. *et al.* De novo design of a transmembrane Zn2+-transporting four-helix bundle. *Science* **346**, 1520-1524 (2014).
12 Vorobieva, A. A. *et al.* De novo design of transmembrane β barrels. *Science* **371** (2021).
13 An, L. *et al.* Binding and sensing diverse small molecules using shape-complementary pseudocycles. *Science* **385**, 276-282 (2024).
14 Berhanu, S. *et al.* Sculpting conducting nanopore size and shape through de novo protein design. *Science* **385**, 282-288 (2024).
15 Scott, A. J. *et al.* Constructing ion channels from water-soluble alpha-helical barrels. *Nat Chem* **13**, 643-650 (2021).
16 Niitsu, A., Heal, J. W., Fauland, K., Thomson, A. R. & Woolfson, D. N. Membrane-spanning α-helical barrels as tractable protein-design targets. *Philos Trans R Soc Lond B Biol Sci* **372** (2017).
17 Chen, X., Dai, X. & Lu, P. Protein design and RNA design: Perspectives. *Quantitative Biology* **14** (2025).
18 Shi, Y. Common Folds and Transport Mechanisms of Secondary Active Transporters. *Annual Review of Biophysics* **42**, 51-72 (2013).
19 Drew, D. & Boudker, O. Shared Molecular Mechanisms of Membrane Transporters. *Annual Review of Biochemistry* **85**, 543-572 (2016).
20 Drew, D., North, R. A., Nagarathinam, K. & Tanabe, M. Structures and General Transport Mechanisms by the Major Facilitator Superfamily (MFS). *Chemical Reviews* **121**, 5289-5335 (2021).
21 Rapp, M., Granseth, E., Seppälä, S. & von Heijne, G. Identification and evolution of dual-topology membrane proteins. *Nature Structural & Molecular Biology* **13**, 112-116 (2006).
22 Grigoryan, G. & DeGrado, W. F. Probing designability via a generalized model of helical bundle geometry. *Journal of molecular biology* **405**, 1079-1100 (2011).
23 Thomson, A. R. *et al.* Computational design of water-soluble alpha-helical barrels. *Science* **346**, 485-488 (2014).
24 Huang, P. S. *et al.* High thermodynamic stability of parametrically designed helical bundles. *Science* **346**, 481-485 (2014).
25 Dauparas, J. *et al.* Robust deep learning–based protein sequence design using ProteinMPNN. *Science* **378**, 49-56 (2022).
26 Daley, D. O. *et al.* Global topology analysis of the Escherichia coli inner membrane proteome. *Science* **308**, 1321-1323 (2005).
27 Jumper, J. *et al.* Highly accurate protein structure prediction with AlphaFold. *Nature* **596**, 583-589 (2021).

28 Krogh, A., Larsson, B., von Heijne, G. & Sonnhammer, E. L. Predicting transmembrane protein topology with a hidden Markov model: application to complete genomes. *J Mol Biol* **305**, 567-580 (2001).

29 Eberhardt, J., Santos-Martins, D., Tillack, A. F. & Forli, S. AutoDock Vina 1.2.0: New Docking Methods, Expanded Force Field, and Python Bindings. *J Chem Inf Model* **61**, 3891-3898 (2021).

30 Shimizu, Y. *et al.* Cell-free translation reconstituted with purified components. *Nature Biotechnology* **19**, 751-755 (2001).

31 Yandrapalli, N., Seemann, T. & Robinson, T. On-Chip Inverted Emulsion Method for Fast Giant Vesicle Production, Handling, and Analysis. *Micromachines* **11**, 285 (2020).

32 Cabantous, S., Terwilliger, T. C. & Waldo, G. S. Protein tagging and detection with engineered self-assembling fragments of green fluorescent protein. *Nature Biotechnology* **23**, 102-107 (2005).

33 Yan, N. Structural Biology of the Major Facilitator Superfamily Transporters. *Annu Rev Biophys* **44**, 257-283 (2015).

34 Radestock, S. & Forrest, L. R. The alternating-access mechanism of MFS transporters arises from inverted-topology repeats. *Journal of molecular biology* **407**, 698-715 (2011).

Figure legends:

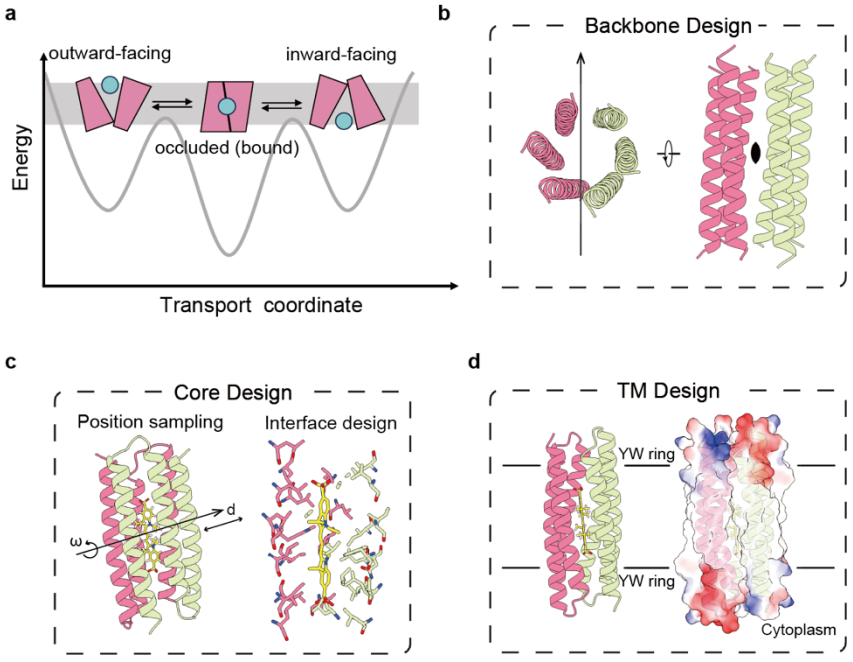

Figure 1 | Design principles of dual-topology membrane transporters.

a, The conformational energy landscape of dual-topology membrane transporters. Dynamic structural rearrangements of membrane transporters were illustrated, cycling through distinct conformational states—such as inward-facing, occluded, and outward-facing. The dual-topology architecture ensures balanced free energies between inward- and outward-facing states, facilitating efficient conformational switching. The symmetric occluded state bound to a ligand reduced the energy barrier for ligand translocation. **(b-d)** Design approach for dual-topology membrane transporters. **b**, Parametric design of antiparallel dimeric three-helix bundles. The C2 symmetry axis and the resulting helical bundle are shown in two different views, with one protomer colored in pink and the other in yellow. **c**, Sampling the ligand position and designing the protein-ligand interactions. Two degrees of freedom were sampled for the small-molecule Cy3 dye: rotation and translation along the C2 symmetry axis of the helical bundle. The Cy3 dye and its interacting residues were depicted as sticks. **d**, Design of transmembrane span. Two rings of amphipathic aromatic residues (Y/W) were designed at positions corresponding to the putative lipid–water interface to promote the formation of a dual topology.

All structural images were generated by using ChimeraX-1.6.1.

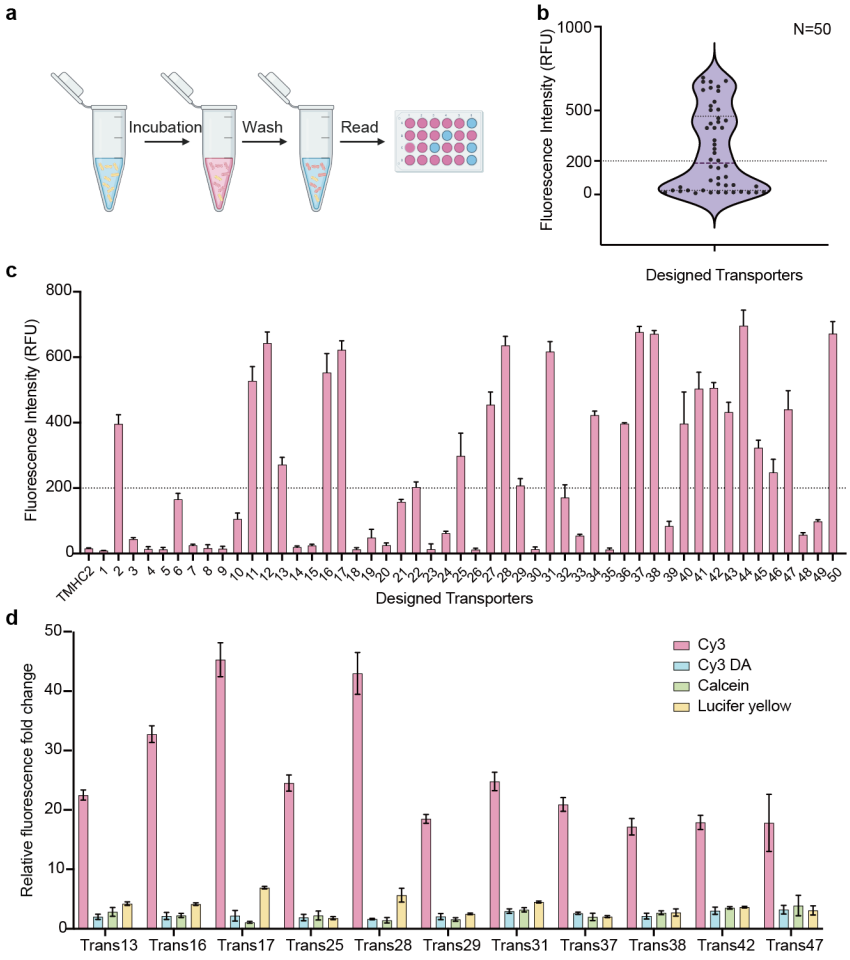

Figure 2 | Functional screening of designer transporters using a cell-based dye uptake assay.

a, Scheme of the transport assay. *E. coli* cells expressing different designs were incubated with 1 mM Cy3 dye solution and then washed with PBS buffer, the resulting accumulation of the Cy3 dye within the cells was monitored by measuring the fluorescence. **b,** Distribution of Cy3 uptake levels across 50 designs shown in a violin plot, where the upper, middle, and lower dashed lines denote third quartile, median, and first quartile, respectively. A dashed line indicating an RFU value of 200 was shown. **c,** Cy3 accumulation levels for various designer transporters, with the non-functional structural protein TMHC2 serving as a negative control. **d,** Relative transport efficiency of multiple small-molecule dyes with diverse chemical structures for 11 randomly selected designs that exhibit Cy3 transport activity. Chemical structures of the dyes used in this study were shown.

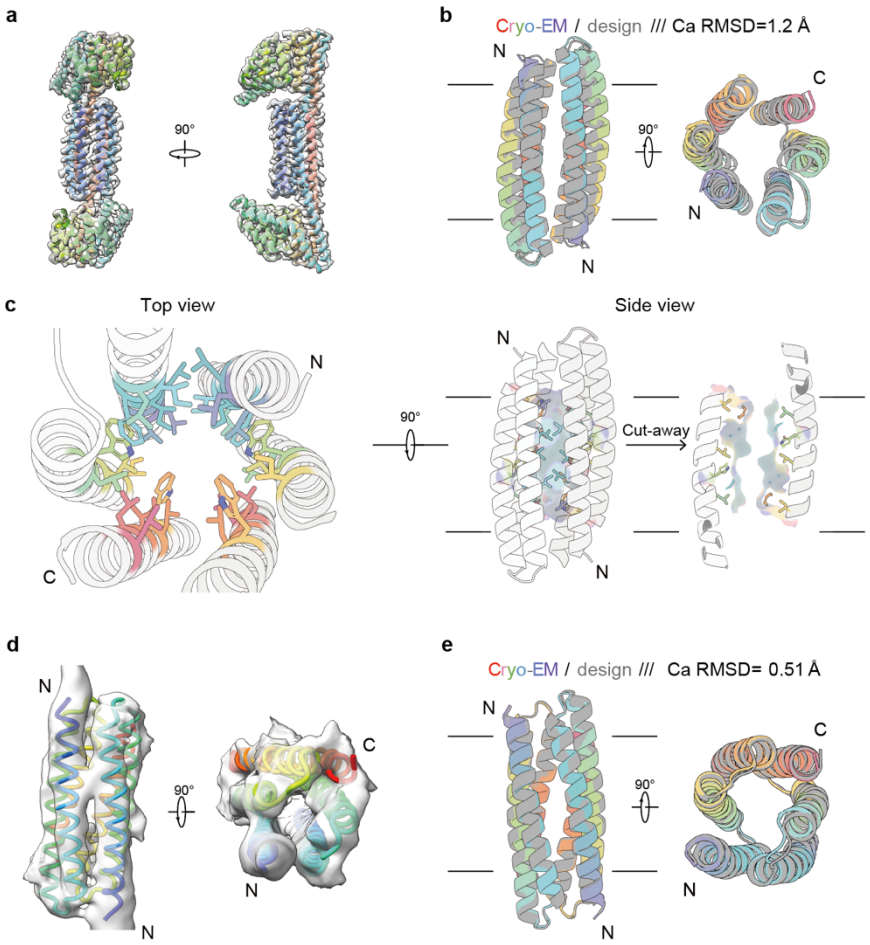

Figure 3 | Cryo-EM structure of designer transporters.

a, Two views of the cryo-EM structure of Trans25_sol (colored in rainbow) overlaid with its corresponding cryo-EM density map (gray), contour level 0.55. **b,** Structural alignment of the transmembrane domain of Trans25_sol from cryo-EM (rainbow) with the original design model (gray). **c,** Close-up views of the putative ligand-binding site in the Trans25_sol structure, with surrounding residues shown as stick. **d,** Two views of the cryo-EM density map (gray) and the fitted cryo-EM structure (rainbow) of Trans42_TM with density contoured at 0.09. **e,** Structural superposition of the transmembrane domain of Trans42_TM from cryo-EM (rainbow) and the design model (gray).

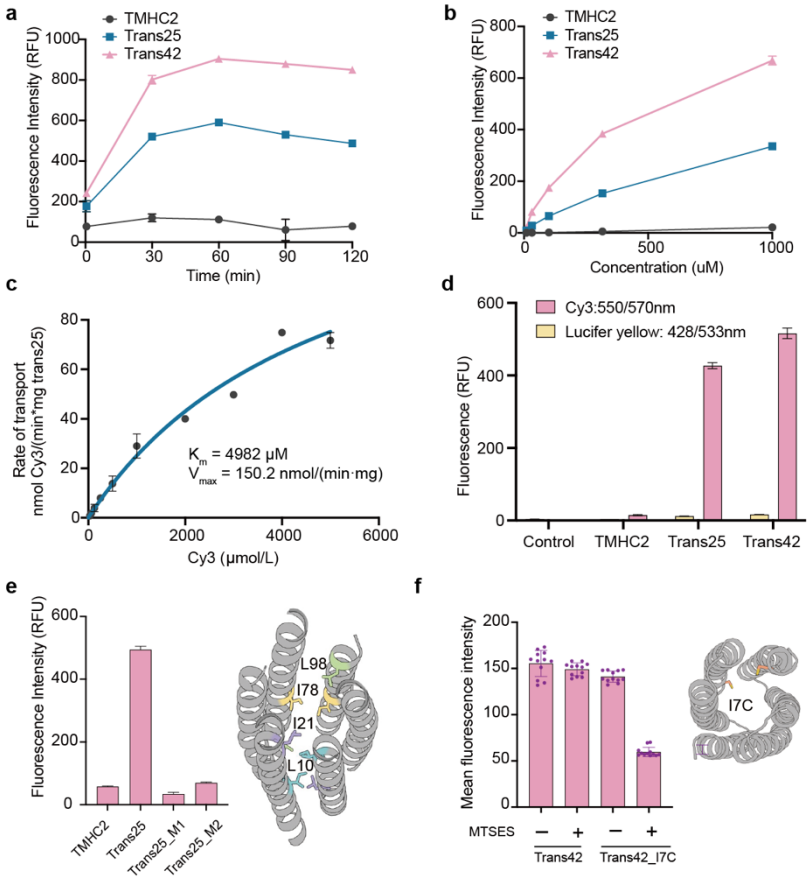

Figure 4 | Functional characterization of designer transporters.

a, Time dependence of Cy3 accumulation in *E. coli* cells expressing the designer transporters. The cells were incubated with Cy3 for the specified durations, after which transport was stopped by centrifugation and washing. **b,** Concentration-dependent Cy3 accumulation in the cell-based dye uptake assay. Cells were incubated with varying concentrations of Cy3 dye to assess uptake efficiency as a function of substrate concentration. **c,** Determination of V_{max} and K_m for Trans25-mediated Cy3 transport. Transport rates were measured at 10 different Cy3 concentrations, with Cy3 accumulation quantified after 60 seconds to estimate initial uptake rates. Protein expression levels were estimated using immunoblotting, with signal intensity calibrated against a standard of transporter protein with known concentration. **d,** In the presence of both Cy3 and Lucifer yellow in the solution, Trans25 and Trans42 selectively transport Cy3. **e,** Point mutations in Trans25 abolished Cy3 transport. Mutation of putative ligand-binding residues (shown as sticks in different colors) does not allow apparent transport of Cy3. Trans25_M1, Trans25 bearing L10E, I21E, and I87E mutations. Trans25_M2, Trans25 bearing L10E, I21E, and L98E mutations. Shown here is

the total accumulation of Cy3 in the *E. coli* cells. **f,** Chemical modification of the Trans42_I7C mutant decreased Cy3 transport. Treatment with the negatively charged reagent MTSES reduced Cy3 accumulation in Trans42_I7C but had no effect on Trans42 in control experiments. The mutated cysteine residues are depicted as sticks.

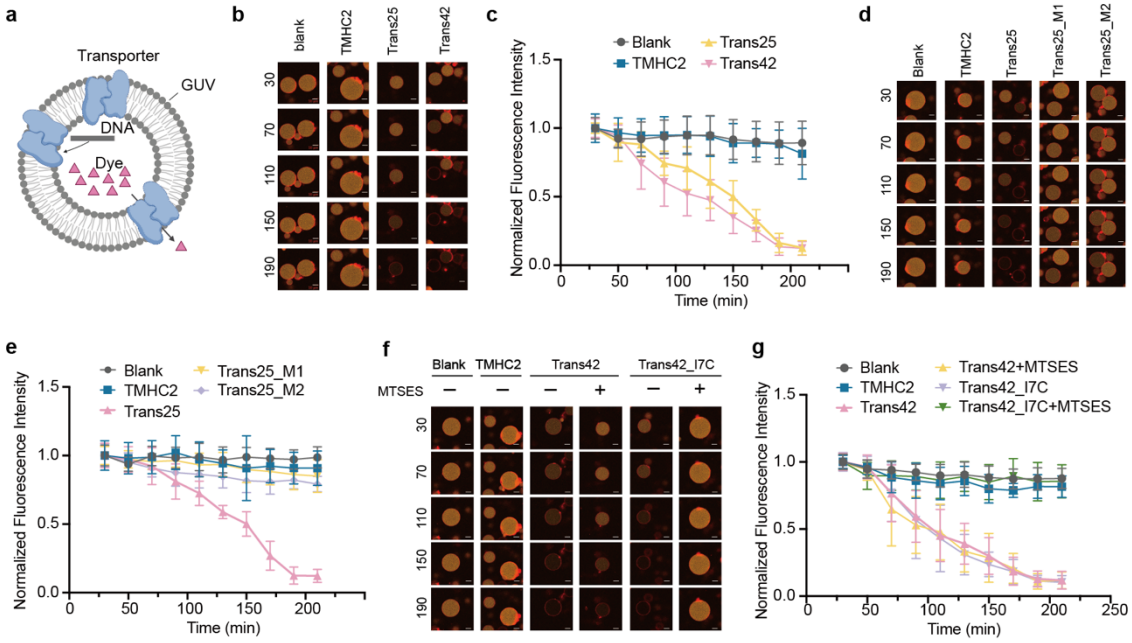

Figure 5 | Characterization of Cy3 transport in Giant Unilamellar Vesicles.

a, Schematic of the assay: DNA encoding membrane proteins was co-encapsulated with the PUREfrex system and Cy3 dye inside GUVs. Successful expression and membrane insertion of functional transporters result in Cy3 efflux. **(b–c)**, Representative time-lapse images (**b**) and corresponding Cy3 fluorescence quantification (**c**) of GUVs expressing an empty vector (Blank), the negative control protein TMHC2, or the designed transporters Trans25 and Trans42. (**d–e)**, Representative images (**d**) and fluorescence traces **(e)** of GUVs expressing functional Trans25 compared to its non-functional mutants. Trans25_M1, Trans25 bearing L10E, I21E, and I87E mutations. Trans25_M2, Trans25 bearing L10E, I21E, and L98E mutations. **(f–g)**, Representative images (**f**) and fluorescence quantification (**g**) of GUVs expressing Trans42 and its I7C mutant in the presence or absence of MTSES. For all plots, traces represent data collected from n=10 independent GUVs. All confocal images share a scale bar of 10 μm.

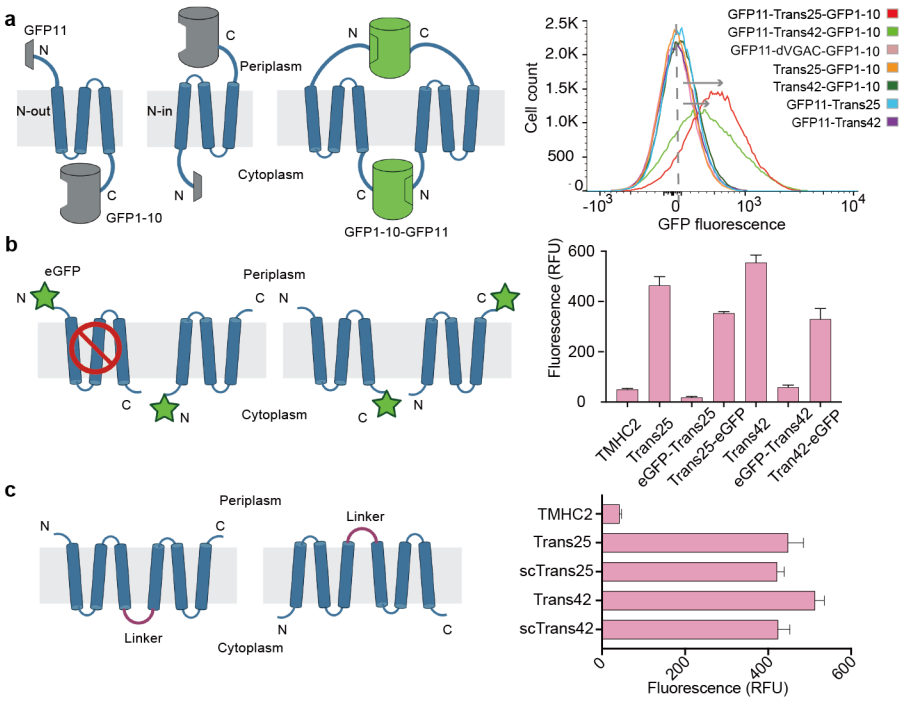

Figure 6 | Characterization of transmembrane topology of designer transporters.

a, In the split GFP complementation assay in *E. coli*, Trans25 or Trans42 fused to GFP11 at the N-terminus and GFP1–10 at the C-terminus produced strong fluorescence, indicating dual-topology insertion with both termini on the same side of the membrane. No significant signal was observed in controls expressing either fusion alone or the non-dual-topology channel dVGAC with the same tags. **b,** Different tagging strategies affect the proper assembly of the functional transporters. C-terminal eGFP tagging of Trans25 and Trans42 preserved dual-topology insertion and did not disrupt dye transport activity. In contrast, N-terminal eGFP tagging likely interfered with membrane integration of the N_{out} topology, abolishing functional transport. **c,** Single-chain versions of Trans25 and Trans42 exhibited strong dye transport activity, comparable to the original design.

Methods

1. Computational design of dual-topology membrane transporters

1.1 Parametric generation of anti-parallel helices.

Idealized α-helices were generated using the Rosetta BundleGridSampler[28] based on Crick coiled-coil parameterization. The following parameters were sampled: the super helical twist (w_0), the major helix radius (r_0), the rotation about the helix's own axis ($\Delta\omega_0$), and the starting helical phase ($\Delta\omega_1$). For each model, three helices were independently sampled for w_0, r_0, $\Delta\omega_0$, $\Delta\omega_1$, and the tilt angle (θ) of the α-helix around the x-axis. Anti-parallel topology was generated by applying a twofold (C2) symmetry operation about the x-axis, with the bundle's super helical axis aligned along z.

Each helix comprised 30 residues, providing a total length sufficient for spanning a typical transmembrane region. In total, 27,783,000 parameter combinations were enumerated under C2 symmetry. Models exhibiting backbone clashes or lacking pore-like geometry were filtered out. The remaining scaffolds were subjected to sequence design using ProteinMPNN[25] with C2 symmetry, and 146,911 designs passed subsequent designability filtering.

1.2 Symmetric ligand docking.

The 3D conformer of Cy3 (diso3, di et) (abbreviated as Cy3) was obtained from *PubChem* and subsequently optimized in *Avogadro* to yield a chemically valid, fully symmetric structure. A Rosetta-compatible parameter (.params) file was generated for the ligand. The optimized Cy3 molecule was then symmetrically docked onto the parametrically generated helical scaffolds. Both the protein scaffold and ligand shared the x-axis as the symmetry axis, and the ligand was sampled by small translations and rotations relative to this axis. In total, 3,525,552 docking configurations were generated.

1.3 Pocket design.

After ligand docking, each scaffold was threaded with the sequence generated during the "1.1 Parametric generation of anti-parallel helices" step. Pocket residues packing was performed in Rosetta under C2 symmetry, allowing simultaneous optimization of both subunits while

maintaining structural equivalence. During the design stage, backbone flexibility was restricted by applying coordinate constraints to the Cα atoms, and tryptophan residues were disfavored with a weight of 1.0. The resulting pocket designs were filtered based on multiple structural and energetic criteria: contact molecular surface area > 250 Å², Rosetta $\Delta\Delta G < -35$, shape complementarity > 0.65, and fewer than three buried unsatisfied polar atoms—yielding 79,650 designs (n = 79,650) that passed all filters.

1.4 Loop connection and sequence design.

Six helices containing pre-organized ligand pockets were assembled into an antiparallel dimer using the Rosetta ConnectChainsMover, in which short rigid loops were constructed to connect adjacent helices.

The prefiltered Rosetta sequences were subsequently optimized using ProteinMPNN with C2 symmetry, while all residues within 5 Å of the ligand were fixed to preserve pocket geometry. All ProteinMPNN-generated sequences were evaluated using AlphaFold2. For each design, five structure predictions were generated, and only those for which all five models satisfied the following criteria were retained: pLDDT > 90, Cα RMSD < 1.0 Å, and pocket RMSD < 0.6 Å relative to the corresponding Rosetta model. Designs passed these filters were selected for subsequent conversion into transmembrane architectures.

For membrane embedding, the hydrophobic transmembrane (TM) span and the tryptophan–tyrosine ("WY") anchoring ring were sampled over lengths ranging from 21 to 35 Å (1 Å intervals). The sequences within the TM span were redesigned using a Rosetta fixed-backbone design protocol under defined compositional constraints: only Leu, Ile, Val, Ala, Met, and Phe were allowed; the Leu and Ile fractions were restricted to 0.15–0.4, Val to 0.15–0.3, Ala to 0.05–0.15, and at most one Met residue per model. Extramembrane surface residues were further refined through rational design to facilitate WY-ring formation, thereby locking the transmembrane dimer into the correct register within the membrane. Throughout this process, the same pocket criteria used in section 1.3 were applied to ensure that the ligand-binding pockets remained intact in the redesigned models.

1.5 Evaluation via TMHMM, AlphaFold2, and MMseq2

Membrane protein topology was predicted using TMHMM 2.0. Designs were considered capable of adopting dual orientations in the cellular membrane if the predicted N_{in} probability fell between 0.3 and 0.7.

AlphaFold2 (AF2) predictions were performed using a local installation of ColabFold 1.3.0 for both pocket design evaluation and final model evaluation. AF2 was run in single-sequence mode with five recycles, and all five output models for each design were used for validation. Designs were retained only if all five models satisfied the following criteria: pLDDT > 90, Cα RMSD < 0.8 Å, and pocket RMSD < 0.4 Å relative to the corresponding Rosetta model.

After redundancy removal using MMseqs2, a total of 216 designs passed, and 50 designs were selected for downstream experimental characterization.

2. Computational design of rigid auxiliary domains for structural determination

To facilitate cryo-EM structure determination of the designed transporters, we engineered three classes of soluble fusion partners, each connected to the transporter via computationally designed rigid linkers.

2.1 MBP and MBP-binding protein fusion design.

Maltose-binding protein (MBP) and the high-affinity MBP-binding designed ankyrin-repeat protein off7 (DARPin_off7) were used as an orthogonal binding pair. The N-terminal helix of transporter candidate was computationally extended using the Rosetta Remodel mover to form a rigid helical fusion with the C-terminal helix of MBP. At the C terminus of the transporter, a sufficiently long Gly–Ser flexible linker was introduced to connect to DARPin_off7. During ProteinMPNN sequence design, the amino-acid identities of MBP, DARPin_off7, and the transporter sequences were held fixed; only linker residues were optimized. All fusion designs were evaluated using AlphaFold2.

2.2 BRIL fusion design.

The thermostabilized apocytochrome b562 (BRIL), a four-helix bundle frequently used to assist GPCR structure determination, was incorporated as a rigid fusion domain. In our case, BRIL was inserted into selected loop regions of the transporters through two rigid helical linkers. The relative

orientation between BRIL and the transporter, as well as the linker geometry, was generated using RFdiffusion with BRIL structure is inpainted. Linker sequences were subsequently sampled with ProteinMPNN under C2 symmetry constraints, and all designed constructs were validated using AlphaFold2.

2.3 De novo soluble domain fusion design.

De novo soluble proteins were fused to loop regions of the target proteins via two rigid linkers. These de novo domains ranged from 200 to 300 amino acids in length. Both the domains and linkers were generated simultaneously using RFdiffusion, and side-chain identities were designed with ProteinMPNN under C2 symmetry. Designed sequences were then evaluated and filtered using AlphaFold2.

3. AutoDock Vina validation

Docking validation was performed using AutoDock Vina (v1.2.7). Input structures were prepared in PDBQT format using the standard preparation scripts provided in the AutoDock Vina repository from https://github.com/ccsb-scripps/AutoDock-Vina. The ligand structure used for docking was identical to that employed in the Rosetta-based design calculations. Docking simulations were carried out using the Vina scoring function, with the search space defined to encompass the full ligand-binding pocket. All remaining parameters were kept at their default settings.

4. Experimental materials and methods

4.1 Dyes preparation.

Cy3 (CAS: 765265-69-8; excitation/emission: 550/570 nm) was prepared in PBS at a final stock concentration of 25 mM. Cy3 DA (CAS: 146397-17-3; excitation/emission: 550/570 nm) was dissolved in PBS to obtain a 20 mM stock solution. Lucifer yellow (CAS: 77944-88-8; excitation/emission: 428/533 nm) was prepared in PBS at a final concentration of 20 mM. Calcein (CAS: 1461-15-0; excitation/emission: 501/521 nm) was dissolved in PBS to yield a 1 mM stock solution.

4.2 Cloning and expression.

The designed genes were synthesized by Beijing Tsingke Biotech Co., Ltd. and subcloned into the pBAD vector and were transformed individually into *E. coli* BW27783. Single colonies were selected and grown overnight in LB medium containing ampicillin. Overnight cultures were diluted into fresh LB and grown to an OD_{600} of 1.0–1.2, followed by induction with 0.04% (w/v) L-arabinose (CAS: 5328-37-0) and incubation at 18 °C for 20 h.

For recombinant protein production, the designed genes encoding the protein of interest fused to various fusion domains, along with a C-terminal hexahistidine (6×His) tag, were cloned into the pET29b vector. To enhance protein expression and achieve proper membrane localization with dual-topology, two N-terminal fusions of the designer transporter with maltose-binding protein (MBP) — one version including the MBP signal peptide and the other lacking it — were co-expressed. Overnight *E. coli* cultures were diluted into fresh LB medium and grown to an OD_{600} of ~0.8. Expression was induced with 200 μM IPTG (CAS: 367-93-1) and cultures were incubated at 18 °C for 20 h.

4.3 Fluorescence-based transport assays in *E. coli*.

4.3.1 General transport assay.

For most constructs, transport activity was measured as follows. Cells were harvested, washed with PBS, and resuspended in M9 medium supplemented with 0.4% (w/v) glucose to an OD_{600} of 10. Cy3 dye was added to a final concentration of 1 mM, and the cell suspension was incubated at room temperature for 1 h. Cells were then collected by centrifugation at 12,000 rpm for 1 min, washed twice with PBS, resuspended in 100 μL PBS, and transferred to black 96-well plates. Fluorescence was measured in triplicate.

4.3.2 Preliminary screening of Cy3 transporters.

Preliminary screening was performed using the general transport assay described in Section 5.3.1, except that the incubation time with Cy3 was extended to 4 h. Fluorescence was measured in triplicate.

4.3.3 Substrate specificity assay.

Cells were prepared as described in Section 5.3.1 and incubated separately with Cy3, Cy3 DA, Lucifer yellow, or Calcein (1 mM each) for 1 h at room temperature. Fluorescence was measured in triplicate.

4.3.4 Time-course and concentration-dependent assays.

Cells were prepared as described in Section 5.3.1. For time-course assays, cells were incubated with 1 mM Cy3 at room temperature for 0, 0.5, 1, 1.5, and 2 h. For concentration-response assays, cells were incubated with Cy3 at 0, 50, 100, 250, 500, or 1,000 μM for 1 h at room temperature. Fluorescence was measured in triplicate.

4.3.5 Kinetic analysis.

Cells were prepared as described in Section 5.3.1 and incubated with Cy3 at concentrations ranging from 31.25 to 5,000 μM for 1 min. Cells were then rapidly washed with PBS, and fluorescence was measured in triplicate. The cumulative substrate amount and transporter protein levels were determined using a Cy3 fluorescence standard curve and immunoblotting, respectively. Kinetic parameters (K_m, V_{max}, and k_{cat}) were obtained by fitting the data to the Michaelis–Menten equation using GraphPad Prism.

4.3.6 Dye competition assay.

Cells were prepared as described in Section 5.3.1 and incubated with a mixture of Cy3 and Lucifer yellow (1 mM each) for 1 h at room temperature. Fluorescence of Cy3 and Lucifer Yellow was measured separately in triplicate.

4.3.7 Transport assays in *E. coli* BL21(DE3).

TMHC2, Trans25, and Trans42 were cloned into pET29b and transformed into BL21(DE3). Cells were induced with 100 μM IPTG for 20 h at 18 °C and assayed for transport activity using the general transport protocol described in Section 5.3.1.

4.4 Transport blocking assay using MTSES reagent.

Overnight cultures (200 μL) of TMHC2, Trans42, and Trans42_I7C were inoculated into 20 mL LB medium and grown at 37 °C until OD_{600} reached 0.4–0.5. A 6 mL aliquot was then transferred

into 54 mL pre-warmed LB medium (37 °C), and Cephalexin was added to a final concentration of 60 μg/mL. Protein expression was induced with 0.01% (w/v) L-arabinose, and cultures were incubated for 1 h at 37 °C. Cells were harvested by centrifugation at 3,000 g for 5 min, washed once with PBS, and resuspended in PBS to an OD_{600} of 10.

For fluorescence imaging, cells were treated with or without 5 mM MTSES (Anatrace; CAS: 184644-83-5) for 15 min at room temperature, followed by the addition of Cy3 (50 μM). Imaging was performed on a Zeiss LSM 980 microscope using a 20× objective. Cy3 fluorescence was excited with a 548 nm laser, and all images were processed using ZEN Microscopy Software (Zeiss). Fluorescence intensity was quantified using ImageJ v2.14.0 by by defining cellular regions of interest (ROIs) using intensity-based thresholding.

4.5 Protein purification.

Induced cells were harvested, resuspended in 30 mL TBS buffer (20 mM Tris–HCl, pH 8.0, 150 mM NaCl) per liter of culture, and disrupted using a high-pressure homogenizer. Cell debris was removed by centrifugation at 10,000 g for 15 min, and the supernatant was further centrifuged at 13,000 rpm for 2 h to isolate the membrane fraction.

The membrane pellet was solubilized in TBS buffer containing 2% (w/v) n-decyl-β-D-maltopyranoside (DM; Anatrace; CAS: 168037-12-5) at 4 °C for 1 h, followed by centrifugation at 13,000 rpm for 30 min. The supernatant was incubated with Ni^{2+}–NTA resin and washed sequentially with 10 mL of TBS buffer containing 30 mM imidazole and 0.05% (w/v) LMNG (Anatrace; CAS: 1257852-96-2), and 20 mL of TBS buffer containing 30 mM imidazole and 0.01% (w/v) LMNG. Proteins were eluted with 10 mL of TBS buffer containing 300 mM imidazole and 0.01% (w/v) LMNG.

Eluted protein was concentrated and further purified by size-exclusion chromatography on a Superdex 200 Increase 10/300 GL column (GE Healthcare) using gel-filtration buffer (20 mM Tris–HCl, pH 8.0, 150 mM NaCl, 0.01% (w/v) LMNG). Fractions were collected based on absorbance at 280 nm and analyzed by SDS–PAGE.

4.6 Circular dichroism measurements.

Circular dichroism (CD) spectra were recorded using a Chirascan V100 spectrometer (Applied Photophysics) in a 0.5 mm path-length cuvette. Protein samples (0.5 mg/mL) were prepared in PBS buffer. Spectra were collected from 180 to 280 nm in triplicate and averaged. Temperature-dependent CD measurements were performed from 25 °C to 95 °C in 2 °C increments, monitoring the signal at 222 nm to generate thermal melts.

4.7 Cryo-EM sample preparation and data acquisition.

Purified protein at a concentration of ~5–15 mg/mL was applied to freshly glow-discharged holey carbon grids (Quantifoil, Au 300 mesh, R1.2/1.3). Grids were blotted for 3.5 s and rapidly plunged into liquid ethane cooled by liquid nitrogen using a Vitrobot Mark IV (Thermo Fisher Scientific) at 100% humidity and 8 °C. Ice thickness and distribution were visually inspected to ensure optimal particle dispersion.

Cryo-EM datasets were acquired on a Titan Krios microscope (Thermo Fisher Scientific) operating at 300 kV, equipped with a Falcon4i detector and a Selectris X energy filter. Images were recorded at nominal magnifications of ×130,000 or ×81,000, corresponding to calibrated pixel sizes of ~0.92 Å and ~0.5435 Å, respectively. Micrographs were collected with a defocus range of -1.0 to -1.3 µm. Each exposure was fractionated into multiple frames to enable motion correction, with a total electron dose of ~50 $e^{-}/Å^{2}$. Data acquisition was performed using EPU software (Thermo Fisher Scientific).

4.8 Cryo-EM data processing.

For Trans25_sol, a total of 4,793 micrographs were collected and binned to a pixel size of 1.087 Å. Dose-weighted micrographs were subjected to contrast transfer function (CTF) estimation in CryoSPARC v4.5.3. Particle picking was performed using a Blob picker, followed by two-dimensional (2D) classification and template-based picking. An ab initio 3D reconstruction was generated and refined using non-uniform refinement. Approximately 686,269 particles contributed to the final map, which achieved an overall resolution of 2.93 Å.

For Trans42_MBP, 27,524 micrographs were acquired. Particles were initially picked with a Blob picker, followed by 2D classification and template-based picking. Multiple rounds of seed-facilitated 2D classification were performed to improve particle selection. Selected particles were

subjected to ab initio 3D reconstruction, and heterogenous refinement was applied to classify remaining particles, yielding a subset of 202,211 particles. This subset was further refined using non-uniform refinement to produce the final map at 3.40 Å resolution.

4.9 Model building and refinement.

For Trans25_sol, the design models were initially refined using CryoNet and subsequently fitted into the corresponding cryo-EM density maps using PHENIX v1.19.2, applying secondary structure, Ramachandran, and rotamer restraints. Iterative manual adjustments were performed in COOT v0.9.5 between rounds of PHENIX refinement.

For Trans42_MBP, the Trans42 design model lacking the fusion domain was refined primarily at the backbone level against the corresponding density map using PHENIX with secondary structure restraints. Manual corrections in COOT were iteratively performed between PHENIX refinement cycles.

4.10 Immunoblotting

Cells were harvested by centrifugation, washed, and resuspended in PBS. Whole-cell lysates were prepared by heating at 95 °C for 5 min and separated on 15% SDS–polyacrylamide gels. Proteins were then transferred onto 0.2 μm nitrocellulose or PVDF membranes for immunoblot analysis.

Membranes were blocked in TBST containing 5% (w/v) nonfat milk for 1 h at room temperature with gentle agitation. FLAG-tagged proteins were detected using a mouse anti-FLAG antibody (ABclonal) at a 1:5,000 dilution. Membranes were incubated with the primary antibody overnight at 4 °C with gentle agitation, washed three times with TBST, and subsequently incubated with an HRP-conjugated goat anti-mouse secondary antibody (Jackson ImmunoResearch, 1:5,000) for 1 h at room temperature. Finally, membranes were developed using the ECL Enhanced Plus Kit (ABclonal).

4.11 Cell-Free Expression and Giant Unilamellar Vesicle (GUV) Assays

Cell-free expression was performed using the Purefrex2.0 kit (GeneFrontier, PF201-0.25-EX) according to the manufacturer's instructions. DNA templates were prepared by linearizing the corresponding plasmids with Q5® High-Fidelity 2X Master Mix (New England Biolabs, M0492L)

using primers T7P-F (CCCGCGAAATTAATACGACTCA) and T7P-R (CGGATATAGTTCCTCCTTTCAG). The inner solution consisted of the Purefrex2.0 components, linearized DNA, and Ficoll® PM70 (Sigma-Aldrich, F2878) at a user-defined concentration.

GUVs were prepared using a lipid mixture of POPC (20 mg/mL, Avanti Polar Lipids, 850457), POPG (20 mg/mL, Avanti Polar Lipids, 840457), and Atto 647N–labeled DOPE (1 mg/mL, Sigma-Aldrich, 42247) at a volumetric ratio of 40:18:0.3, yielding an approximate molar ratio of 7:3 POPC:POPG. Lipids were dried under nitrogen, resuspended in 10 µL decane (Sigma-Aldrich, 457116) and 500 µL mineral oil (Sigma-Aldrich, M5904), and vortexed for 15 min to generate a lipid-oil mixture. The cell-free reaction containing 50 ng linear DNA and 1 mM Cy3 derivative was emulsified by mixing 5 µL of inner solution with 250 µL of the lipid-oil mixture and agitating at 50 Hz for 30 s (Jinxin, Fastprep).

GUVs were formed by layering 200 µL of lipid-oil mixture over 500 µL of outer solution, followed by 200 µL of the emulsion, and centrifuging at 3,000 g for 10 min. The oil phase and supernatant were discarded, and the remaining 100 µL aqueous phase containing GUVs (with 5 mM MTSES in some experiments) was gently transferred to black 96-well glass-bottom plates (Cellvis, P96-1.5H-N) for imaging.

Confocal images were acquired using a Zeiss LSM 980 microscope with a 20× air objective. Fluorescence intensity was quantified using Fiji (v1.53f) and GUV-tracking software (https://github.com/BioProgramming-Lab/GUV-tracking). Vesicles with diameters of 10–30 µm were considered GUVs and included in statistical analyses.

4.12 Split-GFP complementation assay.

Topology was evaluated using a split GFP system. Fusion constructs were generated with a flexible linker (GGSGGGGSGG) between the target protein segment and GFP fragments, including GFP11–Trans25, Trans25–GFP1–10, GFP11–Trans42, Trans42–GFP1–10, GFP11–dVGAC–GFP1–10, GFP11–Trans25–GFP1–10 and GFP11–Trans42–GFP1–10.

For flow cytometry, cells were harvested by centrifugation at 4,000 rpm for 5 min, washed with PBS, and resuspended in 300 μL PBS. Fluorescence was measured on a CytoFLEX flow cytometer (Beckman Coulter) using a green laser, and data were processed and plotted with FlowJo software.

Membrane localization of the fluorescent signals was further examined using a Zeiss 980 microscope in Airyscan mode, with a 63× oil lens.